Draft version January 16, 2019
Typeset using LaTeX **modern** style in AASTeX62

# Possible Detection of Subsecond-Period Propagating Magnetohydrodynamics Waves in Post-Reconnection Magnetic Loops during a Two-Ribbon Solar Flare

Sijie Yu (余思捷 )[1] and Bin Chen (陈彬 )[1]

[1] *Center for Solar-Terrestrial Research, New Jersey Institute of Technology, 323 Martin Luther King Jr. Blvd, Newark, NJ 07102-1982, USA*

(Received Nov 7, 2018; Revised Jan 13, 2019; Accepted Jan 15, 2019)

Submitted to ApJ

## ABSTRACT

Solar flares involve the sudden release of magnetic energy in the solar corona. Accelerated nonthermal electrons have been often invoked as the primary means for transporting the bulk of the released energy to the lower solar atmosphere. However, significant challenges remain for this scenario, especially in accounting for the large number of accelerated electrons inferred from observations. Propagating magnetohydrodynamics (MHD) waves, particularly those with subsecond/second-scale periods, have been proposed as an alternative means for transporting the released flare energy likely alongside the electron beams, while observational evidence remains elusive. Here we report a possible detection of such waves in the late impulsive phase of a two-ribbon flare. This is based on ultra-high cadence dynamic imaging spectroscopic observations of a peculiar type of decimetric radio bursts obtained by the Karl G. Jansky Very Large Array. Radio imaging at each time and frequency pixel allows us to trace the spatiotemporal motion of the source, which agrees with the implications of the frequency drift pattern in the dynamic spectrum. The radio source, propagating at 1000–2000 km $s^{-1}$ in projection, shows close spatial and temporal association with transient brightenings on the flare ribbon. In addition, multitudes of subsecond-period oscillations are present in the radio emission. We interpret the observed radio bursts as short-period MHD wave packets propagating along newly reconnected magnetic flux tubes linking to the flare ribbon. The estimated energy flux carried by the waves is comparable to that needed for accounting for the plasma heating during the late impulsive phase of this flare.

Corresponding author: Bin Chen
bin.chen@njit.edu

*Keywords:* Sun: corona — Sun: flares — Sun: radio radiation — techniques: imaging spectroscopy — waves

## 1. INTRODUCTION

An outstanding question in solar flare studies is how a large amount of magnetic energy released in a flare (up to $10^{33}$ erg) is converted into other forms of energy in accelerated particles, heated plasma, waves/turbulence, and bulk motions, and transported throughout the flare region. The collisional thick-target model (CTTM; Brown 1971), along with the framework of the standard CSHKP flare scenario (Carmichael 1964; Sturrock 1966; Hirayama 1974; Kopp & Pneuman 1976), assumes that a considerable fraction of the released magnetic energy via reconnection goes into acceleration of charged electrons and ions to nonthermal energies in the solar corona (Emslie et al. 2004, 2005, 2012). The downward-propagating electrons along the reconnected, close field lines slam onto the dense chromosphere and lose most of their energy through Coulomb collisions. This sudden energy loss results in the intense heating of the chromospheric material within a confined region at the footpoints of the closed arcades, driving hot and dense material upward and filling the arcades — a process known as "chromospheric evaporation". The arcades, in turn, accumulate a large emission measure at high temperatures, thereby appearing particularly bright in extreme ultraviolet (EUV) and soft X-ray (SXR) wavelengths (see, e.g., a recent review by Benz 2017).

The CTTM model has been successful in accounting for a variety of flare phenomena, most notably the "Neupert effect": The high-energy, hard X-ray (HXR) emission tends to coincide temporally with the rate of the rising lower-energy, SXR emission during the primary energy release phase (also known as the "impulsive phase") of a flare (Neupert 1968; Veronig et al. 2002). Other outstanding examples include the decreasing height (e.g. Brown et al. 2002; Aschwanden et al. 2002; Battaglia & Kontar 2011; Reep et al. 2016) and area (Kontar et al. 2008) of HXR footpoint source with increasing energy. However, significant challenges remain for the CTTM model (see, e.g., Brown et al. 2009 and references therein). One challenge is the so-called "number problem": The total number of nonthermal electrons required to account for the observed HXR, (E)UV, or white light (WL) footpoint sources or flare ribbons can be very large compared to that available in the corona (e.g., Fletcher et al. 2007; Krucker et al. 2011). Similar implications have been made based on observations of coronal HXR sources — the inferred number density of nonthermal electrons is a large fraction of, or in some cases, nearly equal to the total electron density available in the corona (Krucker et al. 2007, 2008, 2010). This requires electrons replenished to the corona at the same rate as non-thermal electrons precipitate from the corona, otherwise the coronal acceleration region would be quickly evacuated. A scenario that invokes return currents, which involve electrons flowing up from the chromosphere

into corona to neutralize the depletion of the coronal electrons, has been suggested to alleviate the difficulty (see, e.g., Hammer & Rostoker 1970; Hoyng et al. 1976; Knight & Sturrock 1977; Emslie 1980; van den Oord 1990; Holman 2012; Alaoui & Holman 2017). Nevertheless, these considerations have led various authors to suggest alternative scenarios that invoke electron (re)acceleration in the lower, denser solar atmosphere (Fletcher & Hudson 2008; Brown et al. 2009; Varady et al. 2014). Other mechanisms have also been proposed for heating the chromospheric plasma, such as thermal conduction or magnetohydrodynamics (MHD) waves (Battaglia et al. 2009; Reep et al. 2016; Reep & Russell 2016). In all cases, alternative means, possibly operating alongside accelerated electrons as in the CTTM model, is postulated to transport a sizable portion of the released flare energy from the reconnection region, presumably located in the corona, downward to spatially-confined regions in the lower solar atmosphere.

One excellent way for providing such focused energy transport other than electron beams is via propagating plasma waves within reconnected flare arcades (Emslie & Sturrock 1982; Fletcher & Hudson 2008; Russell & Stackhouse 2013; Russell & Fletcher 2013). A variety of plasma waves, including Alfvén waves, fast-mode and slow-mode magnetosonic waves, can arise as a natural consequence of the flare energy being released in an impulsive fashion (see, e.g., recent studies by Tarr 2017 and Provornikova et al. 2018). As argued by Fletcher & Hudson (2008) and Russell & Fletcher (2013), plasma waves are capable of carrying a significant amount of flare energy that may be comparable to that needed to power the radiative emissions of a flare. An intriguing recent numerical study by Reep & Russell (2016) demonstrated that the waves can drive chromospheric evaporation in a strikingly similar fashion as electron beams do. Their results were then confirmed by Kerr et al. (2016), who further showed that the detailed shapes of certain chromospheric lines could be used as a potential observational test to distinguish between the wave- and electron-beam heating scenario.

Observationally, flare-associated quasi-periodic pulsations (QPPs) with different periods ranging from <1 second to tens of minutes have been detected at virtually all wavelengths. One of the main origins for the QPPs is thought to be MHD oscillations or waves (see, e.g., Nakariakov & Melnikov 2009 for a review). Observational evidence for large-scale wave-like phenomena associated with flares has also been frequently reported using spatially-resolved imaging data (see reviews by e.g., Patsourakos & Vourlidas 2012; Liu & Ofman 2014; Warmuth 2015; Long et al. 2017, a study of a large sample of such events in Nitta et al. 2013, and a most recent observation of the 2017 September 10 X8.2 flare in Liu et al. 2018). Observational evidence that links the response in the lower solar atmosphere to downward-propagating MHD waves is, however, rather rare. One outstanding example was from Liu et al. (2016), who found a sudden sunspot rotation during the impulsive phase of a flare based on observations from the Goode Solar Telescope of the Big Bear Solar Observatory (GST/BBSO),

possibly triggered by downward-propagating waves generated by the flare energy release. Another interesting study by Brannon et al. (2015) reported long period (∼140 s), slow (∼20 km $s^{-1}$) oscillating flare ribbons based on observations by the Interface Region Imaging Spectrograph (IRIS), although the authors interpreted the oscillating phenomenon in terms of instabilities in the reconnection current sheet rather than MHD waves. It is worthwhile to point out that, in the Earth's magnetosphere, direct evidence for Alfvén waves propagating along the outer boundary of the "plasma sheet" (which is analogous to newly-reconnected flare loops) has been reported based on *in situ* measurements. These waves have been argued to be responsible in transporting a significant amount of energy flux (in the form of Poynting flux) from the energy release site in the magnetotail toward the Earth, which, in turn, powers the auroral emission that is analogous to flare ribbons on the Sun (Wygant et al. 2000; Keiling et al. 2000; Wygant et al. 2002).

Recently, numerical and analytical models have been developed to investigate energy transport and deposition from the corona to the low solar atmosphere by MHD waves (Russell & Fletcher 2013; Reep & Russell 2016; Kerr et al. 2016; Tarr 2017; Reep et al. 2018). An important finding is that short-period MHD waves, especially those having periods of about one second or less, carry a significant amount of energy (Tarr 2017), suffer much less energy loss when propagating out from the corona to the lower solar atmosphere (Russell & Fletcher 2013; Provornikova et al. 2018), and are much more efficient in dissipating the energy in the upper chromosphere comparing to their long-period counterparts (Fletcher & Hudson 2008; Russell & Fletcher 2013; Reep & Russell 2016). Therefore, these short-period MHD waves are thought to be a potential candidate as an alternative carrier for energy released in flares. Subsecond-period ($P < 1$ s) QPPs have been frequently reported in radio and X-ray light curves and/or dynamic spectra (e.g., Rosenberg 1970; Bogovalov et al. 1983; Chen & Yan 2007; Tan et al. 2010; Yu et al. 2013). However, most of the detected large-scale wave-like phenomena based on imaging data fall into the long-period regime (>10 s, e.g., Nakariakov & Melnikov 2009), with some rare exceptions from eclipse observations (e.g., Pasachoff et al. 2002). This is mainly due to the limitation on temporal cadence of current WL/EUV imaging instrumentation, or the lack of radio/X-ray imaging capability at high temporal cadence with sufficient dynamic range or counting statistics.

Here we report ultra-high cadence (0.05 s) spectroscopic imaging of a peculiar type of radio bursts in the decimetric wavelength range ("dm-$\lambda$" hereafter) that is likely associated with propagating subsecond-period MHD waves along flaring arcades. The bursts were recorded by the Karl G. Jansky Very Large Array (VLA) in a GOES-class C7.2 flare that is associated with a failed filament eruption and large-scale coronal EUV waves. We further show that these MHD waves may carry a significant amount of energy flux that is comparable to the average energy flux needed for driving the plasma heating at the flare ribbons. In Section 2, we present VLA dynamic imaging

spectroscopic observations of the radio bursts, supported by complementary magnetic, EUV, and X-ray data. In Section 3, we interpret the observations within a physical scenario that involves propagating short-period MHD wave packets and discuss their energetics. We briefly summarize our findings in Section 4.

## 2. OBSERVATIONS

### 2.1. *Event overview*

The VLA is a general-purpose radio interferometer operating in <1–50 GHz. It has completed a major upgrade (Perley et al. 2011) and was partially commissioned for solar observing in late 2011 (Chen et al. 2013), capable of making broadband radio imaging spectroscopic observations at more than one thousand spectral channels with ultra-high, tens of millisecond-scale time resolution. Recent studies with the VLA have demonstrated its unique power in using coherent solar radio bursts to diagnose the production and transport of energetic electrons in solar flares by utilizing its imaging capabilities with spectrometer-like time and spectral resolution (Chen et al. 2013, 2014, 2015; Wang et al. 2017; Chen et al. 2018a).

The event under investigation occurred on 2014 November 11 in NOAA active region (AR) 12201, located at 44° east from the central meridian. It is a GOES-class C7.2 solar flare (flare identifier "SOL2014-11-01T16:39:00L085C095" following the suggested IAU convention by Leibacher et al. 2010). This event was well observed by the Atmospheric Imaging Assembly (AIA; Lemen et al. 2012) and the Helioseismic and Magnetic Imager (HMI; Scherrer et al. 2012) aboard the Solar Dynamics Observatory (SDO). The impulsive phase of the flare, started from ∼16:39 UT was partially covered by the Ramaty High Energy Solar Spectroscopic Imager (RHESSI; Lin et al. 2002) until 16:42 UT when the spacecraft entered the South Atlantic Anomaly (SAA). The VLA was used to observe the Sun from 16:30:10 UT to 20:40:09 UT and captured the entire flare. The observations were made in frequency bands between 1–2 GHz with 50 ms cadence and 2 MHz spectral resolution in dual circular polarizations. The 27-antenna array was in the C configuration (max baseline length 3 km), yielding an intrinsic angular resolution of $35''.7 \times 16''.3$ at $\nu = 1$ GHz at the time of the observation (and scales linearly with $1/\nu$). The deconvolved synthesis images are restored with a $30''$ circular beam.

Figures 1 and 2 show an overview of the time history and general context of the flare event. The GOES 1–8 Å SXR flux starts to rise at 16:39 UT and peaks at around 16:46 UT, during which a filament is seen to erupt (green arrows in Figure 2) but it does not fully detach from the surface and forms a coronal mass ejection—a phenomenon known as a "failed eruption". During this period, both the HXR light curve (blue curve in Figure 1(D)) and the SXR derivative (red curve in Figure 1(D)) displays multiple bursty features, which is characteristic of the flare impulsive phase during which the primary energy release occurs. Precipitating nonthermal electrons lose most their energy in the dense chromosphere, resulting in HXR sources at the

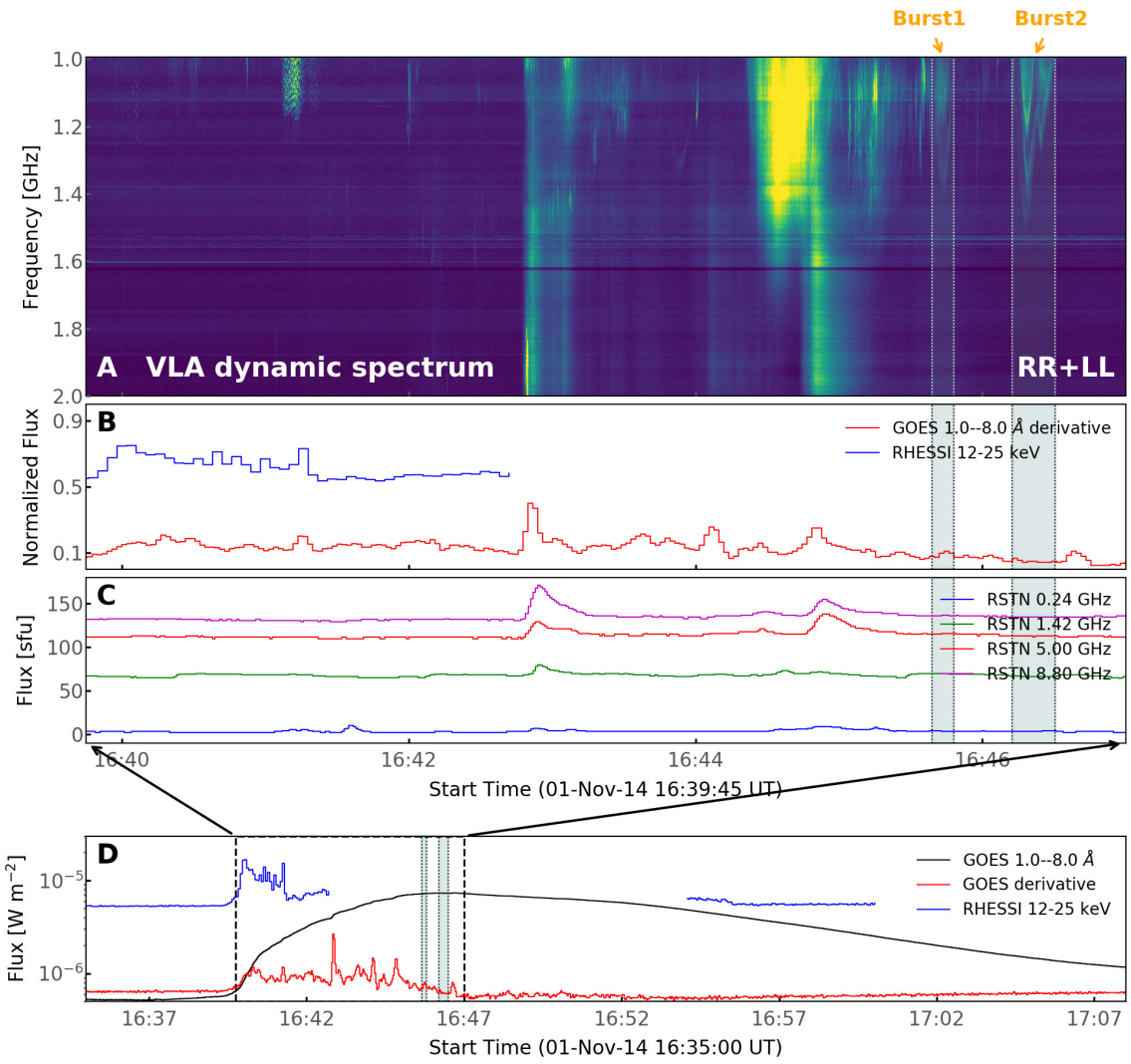


**Figure 1.** (A) VLA cross-power dynamic spectrum at 1-2 GHz of the impulsive phase of the SOL2014-11-01T16:39 Event. The frequency axis is inverted with higher frequency shown at the bottom side. (B) RHESSI 12–25 keV light curve (blue) and the time derivative of the GOES 1–8 Å soft X-ray light curves (red). The periods of the two radio bursts are bracketed by vertical dashed lines. (C) RSTN radio flux at multiple frequencies from 0.24 GHz to 8.8 GHz. (D) GOES and RHESSI light curves of the entire event.

footpoints of the reconnected flare arcades via bremsstrahlung radiation (contours in Figure 2(B)). Bright flare ribbons, visible in UV/EUV passbands (shown in Figure 2 in purple color, which is mostly contributed by AIA 304 Å), are formed due to heating of the chromospheric/photospheric material by precipitated nonthermal electrons or other means. The evaporated chrosmospheric material fills the flare arcades and form bright coronal loops, best seen in EUV passbands that are sensitive to relatively high coronal temperatures (green and blue colors in Figure 2, which show AIA 211 and 94 Å bands that correspond to plasma temperature of 2 MK and 7 MK, respectively). Many of the impulsive peaks in the SXR derivative have counterparts in the Radio Solar Telescope Network (RSTN) light curves (Figure 1(B) and (C)), which are also

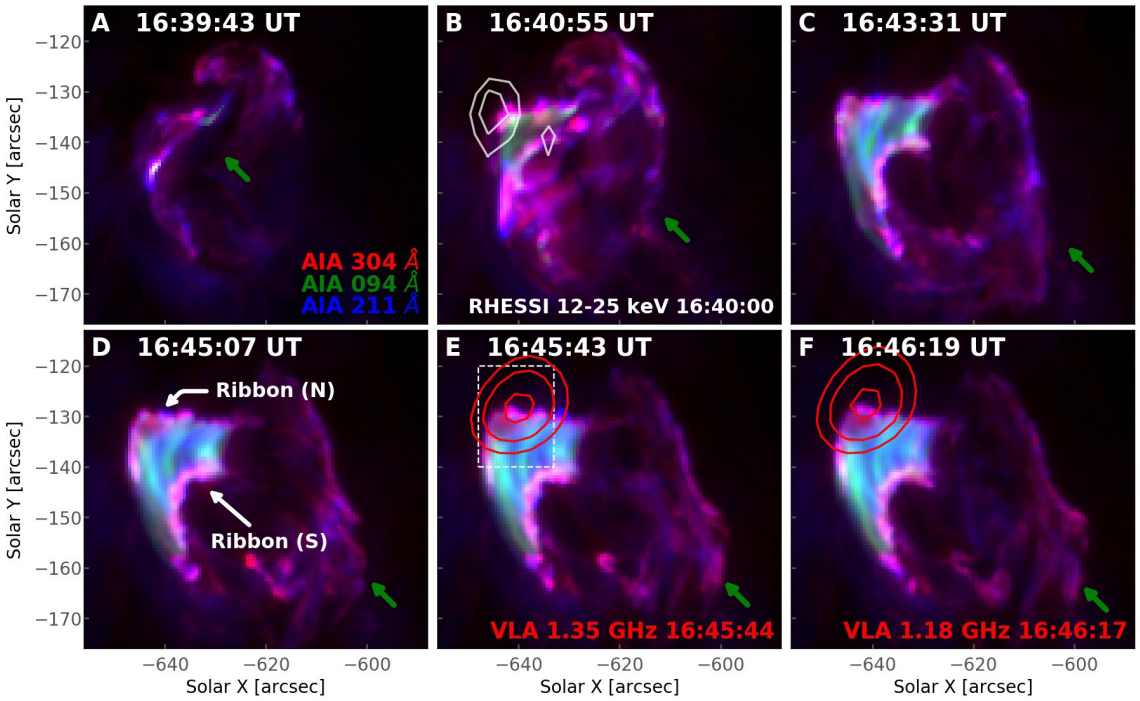


**Figure 2.** Composite EUV image series of SDO/AIA 304 Å (red), 94 Å (green), and 211 Å (blue) EUV bands. The radio sources are shown in red contours at 91 %, 95 % and 99 % of the maximum. White contours are 60 seconds integration of 12-25 keV HXR emission by RHESSI during the early flare impulsive phase. The erupting filament is indicated in (A)–(F) in green arrows, and the two flare ribbons are marked by white arrows in (D). (An animation of this figure is available in the online journal.)

visible in the VLA 1–2 GHz dynamic spectrum as short-duration radio bursts (Figure 1(A)), suggesting that they are both closely associated with accelerated nonthermal electrons. The dm-$\lambda$ bursts have complex fine spectrotemporal structures, especially in the lower-frequency portion of the radio dynamic spectrum.

The radio bursts under study appear during the late impulsive phase (shaded area in Figure 1(A–C) demarcated with vertical dashed lines). Two main episodes can be distinguished in the dynamic spectrum, each of which lasts for ∼10–20 seconds (referred to as "Burst 1" and "Burst 2" hereafter). An enlarged view of these bursts is available in Figures 3(A) and 5(A). From the imaging data, the bursts have a peak brightness temperature $T_B$ of $\sim 1.1\times10^7$ K. The total flux density is $\sim 1$ sfu (solar flux unit; 1 sfu $= 10^4$ Jansky). In addition, the bursts are nearly 100% polarized in left-hand circular polarization (LCP). These properties are consistent with radio emission associated with a coherent radiation mechanism. In the dynamic spectrum, the bursts appear as arch-shaped emission lanes, which display a low-high-low frequency drift pattern. The frequency drift rate $d\nu/dt$ is between 60–200 MHz/s (or a relative drift rate of $\dot{\nu}/\nu \approx 0.04$–$0.2$), which is about one order of magnitude lower than type III radio bursts emitted by beams of fast electrons, but similar to fiber bursts and lace bursts in the same frequency range (Benz & Mann 1998; Karlický et al. 2001; Rausche et al. 2007; Karlický et al. 2013; Wang et al. 2017). Such bursts with an intermediate

frequency drift rates are sometimes referred to as the "intermediate drift bursts" (Benz & Mann 1998; Aurass et al. 2005; Kuznetsov 2006). The multiple episodes of positive- and negative-drifting features, to some extent, resemble the "lace bursts" in the literature (Karlický et al. 2001; Bárta & Karlický 2005; Huang & Tan 2012). However, the emission lanes of these bursts appear to be much smoother, while the lace bursts, at least from the few reported cases in the literature, have a much more fragmentary and chaotic appearance.

Radio imaging of the bursts places the burst source (red contours in Figures 2(E) and (F)) near the northern flare ribbon. The location of the radio bursts is also very close to the RHESSI 12–25 keV HXR footpoint source, shown in Figure 2(B) as white contours, albeit the latter is obtained several minutes earlier (at 16:40 UT) before the spacecraft enters SAA. A more detailed investigation reveals a close temporal and spatial association between the radio bursts and the transient (E)UV brightenings at the northern flare ribbon. Figure 3(B) shows AIA 304 Å background-detrended image sequence during the time interval of the radio dynamic spectrum shown in Figure 3(A). During this period, the northern ribbon is featured by the appearance of two transient EUV brightenings during radio bursts 1 and 2, and the location of the brightenings is very close to the radio source (red). The appearance of the radio source during the flare impulsive phase, as well as its close spatial and temporal association with the ribbon brightenings, suggests that the radio source is intimately related to the release and transport of the flare energy. More detailed discussions of the spectral, temporal, and spatial features of the bursts based on radio dynamic imaging spectroscopy will be presented in the next subsection.

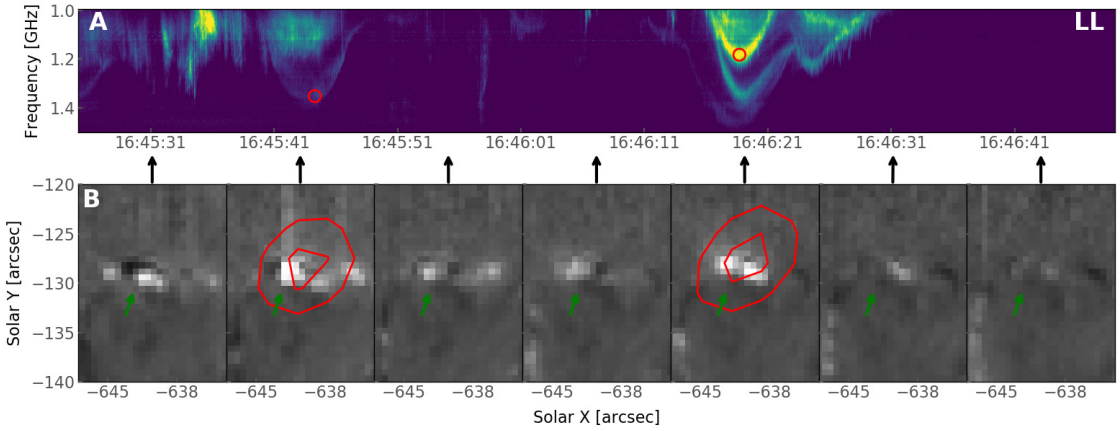


**Figure 3.** (A) VLA cross-power dynamic spectrum in LCP at 1–1.5 GHz obtained from a short baseline. (B) AIA 304Å background-detrended image sequence at times marked by the black vertical arrows in (A), showing the EUV ribbon brightenings near the radio sources. Red contours are the radio images that correspond to Bursts 1 and 2 (the time and frequency are marked in the dynamic spectrum of panel A as red circles; contour levels are 97.5 %, 99.5 % of the image maximum). Green arrows indicate the location of the transient EUV brightening on the north ribbon. The field of view (FOV) is indicated by the dashed box in Figure 2(E).

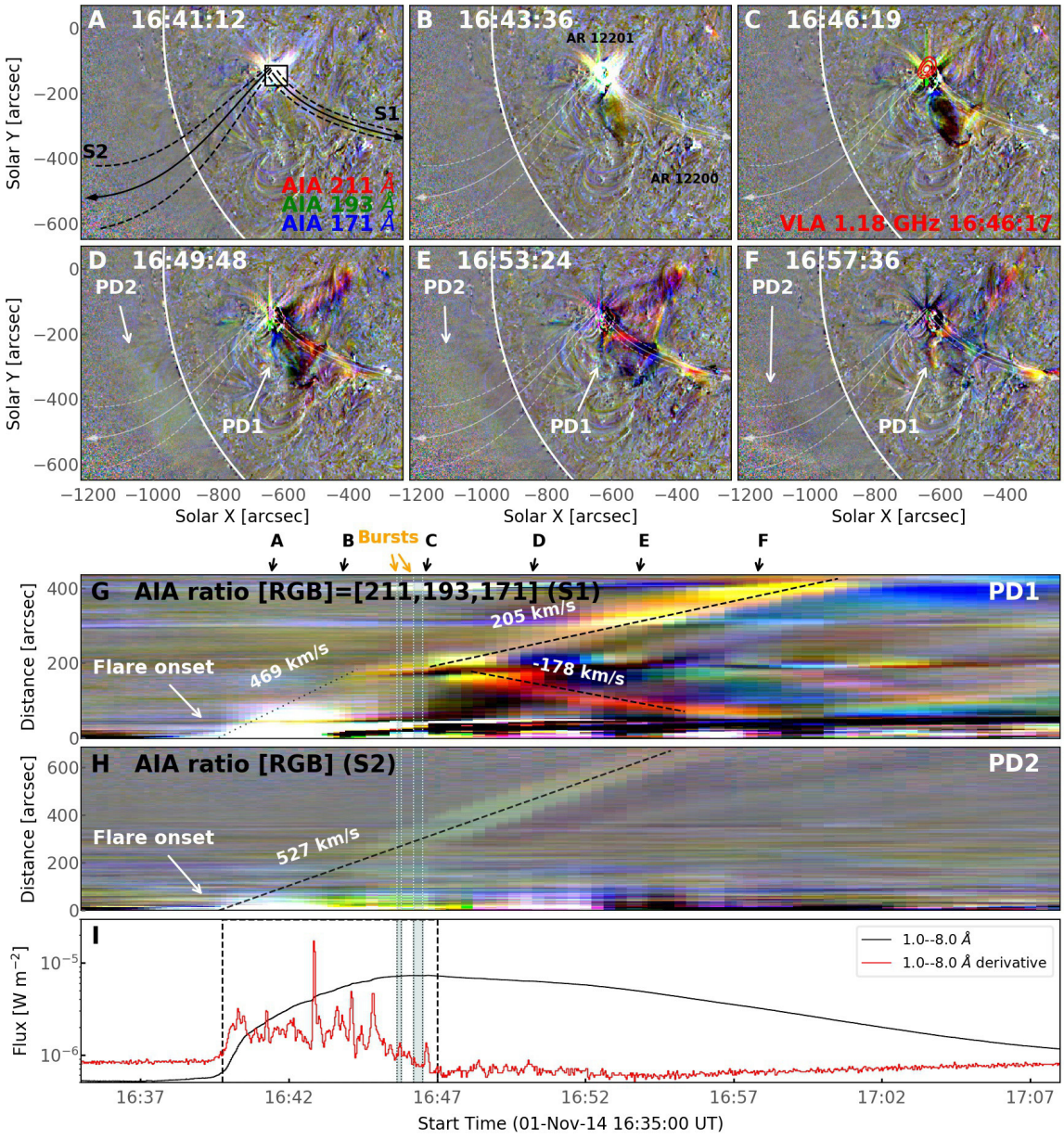


**Figure 4.** Large-scale propagating disturbances observed by SDO/AIA. (A–F) Snapshots of composite AIA 211, 193 and 171 Å running ratio images. The corresponding times of the snapshots are marked by the black arrows above the time-distance plots in (G-H) obtained along two slices in (A) labelled as "S1" and "S2" following the propagation direction of the two large-scale waves. The radio source in (C) is shown as red contours (50 %, 70 % and 90 % of the maximum). The field of view of the EUV images in Figure 2 is indicated by a black box in Panel A. GOES 1–8 Å SXR light curve of the flare and its time derivative are shown in (I). The periods of the two episodes of the radio bursts under study are demarcated by vertical lines in (G-I). (An animation of this figure is available in the online journal.)

Another interesting feature of this event is accompanied with large-scale, fast-propagating disturbances ("PDs" hereafter), observed in EUV, accompanying the impulsive and gradual phase of the flare, which are usually interpreted as propagating MHD waves in the corona (Patsourakos & Vourlidas 2012; Nitta et al. 2013; Liu

& Ofman 2014; Warmuth 2015; Long et al. 2017; Liu et al. 2018). Using AIA 171, 193, and 211 Å running-ratio images (ratio of current frame to a previous frame), a large-scale PD feature (denoted as "PD1" in Figure 4) is present in the area between active region (AR) 12201 and AR 12200. In addition, another large-scale PD appears to move outward above the limb (denoted "PD2" in Figure 4). The temporal evolution of the two PDs is displayed in the time-distance plots in Figure 4(G) and (H), made along two slices labelled as "S1" and "S2" in Figure 4(A), respectively. The initialization of the large-scale PDs coincides with the flare onset, demonstrating their close association with the flare energy release. The large-scale PDs propagate at a speed of 400–500 km $s^{-1}$ with PD1 clearly experiencing multiple deflections by magnetic structures of the ARs. We note that the radio bursts are observed during the period when PD1 remains in the flaring region (Figure 4(C)). This is a strong indication of the presence of ubiquitous MHD disturbances in and around the flaring region during the time of the radio bursts.

### 2.2. *Radio Dynamic Spectroscopic Imaging*

The capability of simultaneous imaging and dynamic spectroscopy offered by the VLA allows each pixel in the dynamic spectrum to form a radio image. As an example, Figure 5(B) shows a three-dimensional (3D) rendering of a VLA spectral image cube taken for Burst 2 within an 100-ms integration (at 16:46:18.2 UT; the timing is shown as the vertical dotted line in panel (A)). The two horizontal slices in Figure 5 (B) indicate the radio images at the peak frequencies of the two emission lanes at that time (circles in panel (A)). The same two radio images are shown in Figures 5(C) and (D) as green and blue contours overlaid on AIA EUV 304 Å image and HMI photospheric line-of-sight (LOS) magnetogram respectively. As discussed in the previous subsection, the radio sources are located near the northern flare ribbon. In the magnetogram, this flare ribbon corresponds to a region with a positive magnetic polarity. As the bursts are 100% LCP, they are likely polarized in the sense of *o* mode.

We produce an independent 3D spectral image cube for each time pixel when the radio burst of interest is present in the radio dynamic spectrum, thereby comprising a four-dimensional (4D) spectotemporal image cube. From the 4D cube we are able to derive the spectrotemporal variation intrinsic to this radio source of interest by isolating its flux from all other sources present on the solar disk in the spatial domain, resulting in a spatial-resolved, or "vector" radio dynamic spectrum of the source (Figure 5(E) and (F)). This technique was first introduced by Chen et al. (2015) based on VLA dynamic spectroscopic imaging data, and was subsequently applied in a number of recent studies with VLA data (Wang et al. 2017; Chen et al. 2018a). A similar approach is discussed in a recent study by Mohan & Oberoi (2017) based on data from the Murchison Widefield Array. The resulted vector dynamic spectra show clearer features of the radio bursts than the cross-power dynamic spectra obtained at

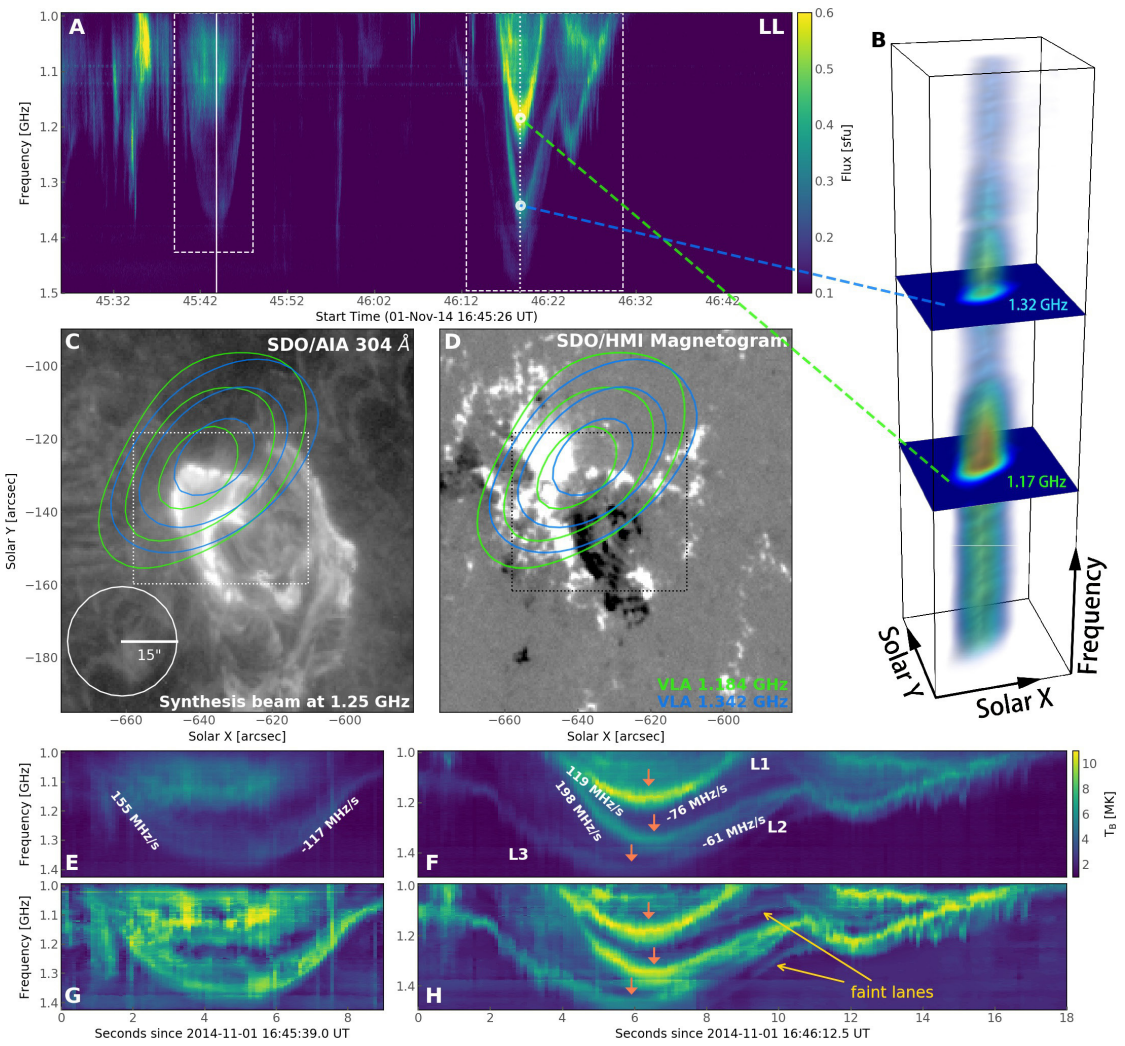


**Figure 5.** (A) VLA cross-power dynamic spectrum in LCP at 1–1.5 GHz obtained from a short baseline. The vertical solid line denotes the frequency turnover time of Bursts 1 and 2. (B) Three-dimension rendering of the spectral image cube of an 100-ms integration snapshot at 16:46:18.2 UT. 256 independent frequency channels are shown. The two horizontal slices indicate radio images at two selected frequencies that correspond to the two intensity peaks at the particular time, shown also in (C) as colored contours overlaid on SDO/AIA EUV 304 Å image at 16:46:19 UT. The contour levels are at 50%, 70% and 90% of the maximum. The circle in (D) represent the size of the restoring beam. (D) Same as C, but the HMI line-of-sight magnetogram is shown as the background. (E-F) Spatially-resolved vector dynamic spectrum of the two burst episodes. (G-H) Feature-enhanced version of the dynamic spectra in panels E-F.

short baselines (which is a proxy of the total-power dynamic spectra; Figure 5(A)). The improvement is, however, not substantial, which is consistent with the imaging results in which this burst source is shown as the dominant emission on the solar disk. To highlight the fine structure of the bursts, we further enhance the vector dynamic spectrum by using the contrast limited adaptive histogram equalization technique (Pizer et al. 1987), shown in Figures 5(G) and (H).

Bursts 1 and 2 share similar spectrotemporal features. They contain at least one emission lane that starts with a positive drift rate toward higher frequency ($d\nu/dt > 0$, sometimes referred to in the literature as "reverse drift" as "normal drift" bursts show negative frequency drifts). It then turns over at the highest frequency point rather smoothly and drifts toward lower frequency with a negative frequency drift rate ($d\nu/dt < 0$). The total frequency variation $\Delta\nu_{\rm tot}/\nu$ can be up to 30%. Burst 2 undergoes two repeated cycles of positive-to-negative frequency drift. At least three distinctive emission lanes are clearly visible (denoted as "L1", "L2", and "L3" in Figure 5(F)) with two additional faint lanes that can only been distinguished in the enhanced dynamic spectrum (arrows in Figure 5(H)). Although the three bright emission lanes of Burst 2 occur closely in time, they differ in their intensity, peak emission frequency, frequency drift rate, and frequency turnover time $t_{\rm o}$ (defined as the time when the emission frequency reaches the highest value and the frequency drift rate $\dot{\nu}$ goes to nearly zero; indicated by red arrows in Figure 5(F) and (H)). The average instantaneous frequency bandwidth $\Delta\nu$ of the emission lanes is about 60–100 MHz, corresponding to a relative frequency bandwidth $\Delta\nu/\nu \approx 6\%$.

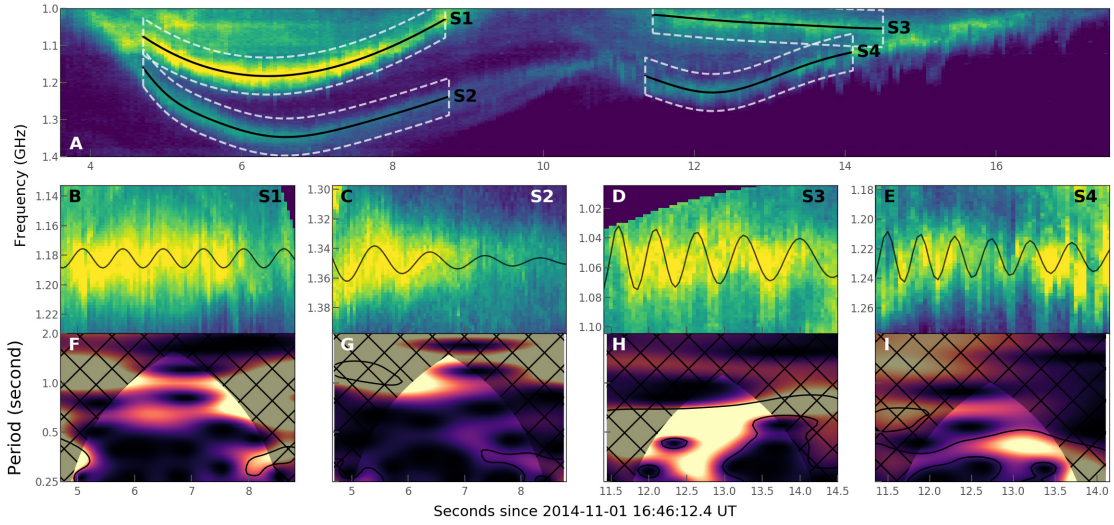


**Figure 6.** Subsecond-scale oscillations in the emission lanes of the dm-$\lambda$ bursts. (A) Full 50-ms time resolution dynamic spectrum of Burst 2. Four segments of emission lanes, labelled "S1", "S2", "S3", "S4", are selected for in-depth analysis shown in B–I. (B–E) Detrended dynamic spectra of the four segments S1–S4. (F–I) Wavelet power spectra of the oscillations for the four segments S1–S4.

More detailed inspection of the dynamic spectral features of the stronger burst (Burst 2; based on the full 50-ms cadence data) reveals multitudes of very short, subsecond-scale fine structures on each emission lane (Figure 6(A)). Figures 6(B–E) provide an enlarged view of four segments of the emission lanes for Burst 2 (labelled as "S1", "S2", "S3", "S4" in Figure 6(A)), which have been detrended to remove their overall frequency drift pattern. The bursts appear to oscillate in their emission

frequency around the central "ridge" of the emission lane quasi-periodically. We use a damped oscillation profile

$$\delta\nu(t) = \delta\nu_0 \exp(-t/\tau_A) \sin\left[\frac{2\pi t}{P/(1-t/\tau_P)^3}\right] \quad (1)$$

to fit the four segments (Figure 6(B–E)). The oscillations have an amplitude of $\delta\nu_0 \approx$ 10–30 MHz (or a relative amplitude of $\delta\nu/\nu$ of ∼1–2%), period of $P \approx 0.3$–1.0 s, and damping times of $\tau_A \approx 0.5$–5 s in amplitude and $\tau_P \gtrsim 30$ s in period. Wavelet analysis of such oscillation patterns in emission frequency confirms that the oscillations display very short, subsecond-scale periods ranging from ∼0.3–1.0 s (Figure 6(F–I)).

Radio imaging of each pixel in the dynamic spectrum where the bursts present provides key information on the spatial variation of the radio source as a function of time and frequency. For each image at a given frequency $\nu$ and time $t$, we fit the source with a 2-D Gaussian function and determine the source centroid $I_{\rm pk}(\theta, \phi, \nu, t)$, where $I_{\rm pk}$ is the peak intensity, and $\theta$ and $\phi$ are the centroid position in helioprojective longitude and latitude. As shown in several previous studies, the uncertainty of the centroid location for unresolved, point-like sources (which is likely the case for the coherent bursts under study) is determined by $\sigma \approx \theta_{\rm FWHM}/{\rm SNR}\sqrt{8\ln 2}$, where $\theta_{\rm FWHM}$ is the FWHM beam width and SNR is the ratio of the peak flux to the root-mean-square noise of the image (Reid et al. 1988; Condon 1997; Chen et al. 2018a). In our data, typical values are $\theta_{\rm FWHM} \approx 30''$ and ${\rm SNR} \gtrsim 20$, which give $\sigma \lesssim 0.6''$. However, as discussed later in Section 3, the bursts are likely associated with fundamental plasma radiation, which is known to be prone to scattering effects as the radiation propagates through the inhomogeneous corona toward the observer (Bastian 1994; Kontar et al. 2017; Chen et al. 2018b; McCauley et al. 2018). Therefore the uncertainty estimate given above should only be considered as a lower limit. In fact, by obtaining the centroid locations of all frequency-time pixels on the emission lane within a small time period (∼0.5 s) and frequency range (∼50 MHz), we find that they are distributed rather randomly within an area of a FWHM size of $\sim 2'' \times 2''$. Hence we estimate the actual position uncertainty of the centroids as $\sigma \approx 1''$.

We focus on Burst 2 for detailed investigations of the spatial, temporal, and spectral variation of the source centroid since it has the best SNR. For each emission lane, firstly, we extract all time and frequency pixels where the intensity exceeds 50% of its peak intensity. An example for such a selection for lane L1 of Burst 2 is shown in Figure 7(A) enclosed by the white contour. Figure 7(B) shows the resulted centroid positions as a function of frequency (as colored dots from blue to red in increasing frequency) for emission lane L1. To further improve positional accuracy and reduce cluttering in the figure, each dot in the plot represents the average position for centroids at all frequency pixels across the emission lane (that have an intensity above 50% of the peak) for a given time $t$, with the color representing their mean frequency. The background of Figure 7(B) is the HMI photospheric magnetogram

shown in grayscale, overlaid with the AIA 1600 Å image. The latter clearly shows the double flare ribbons in red color.

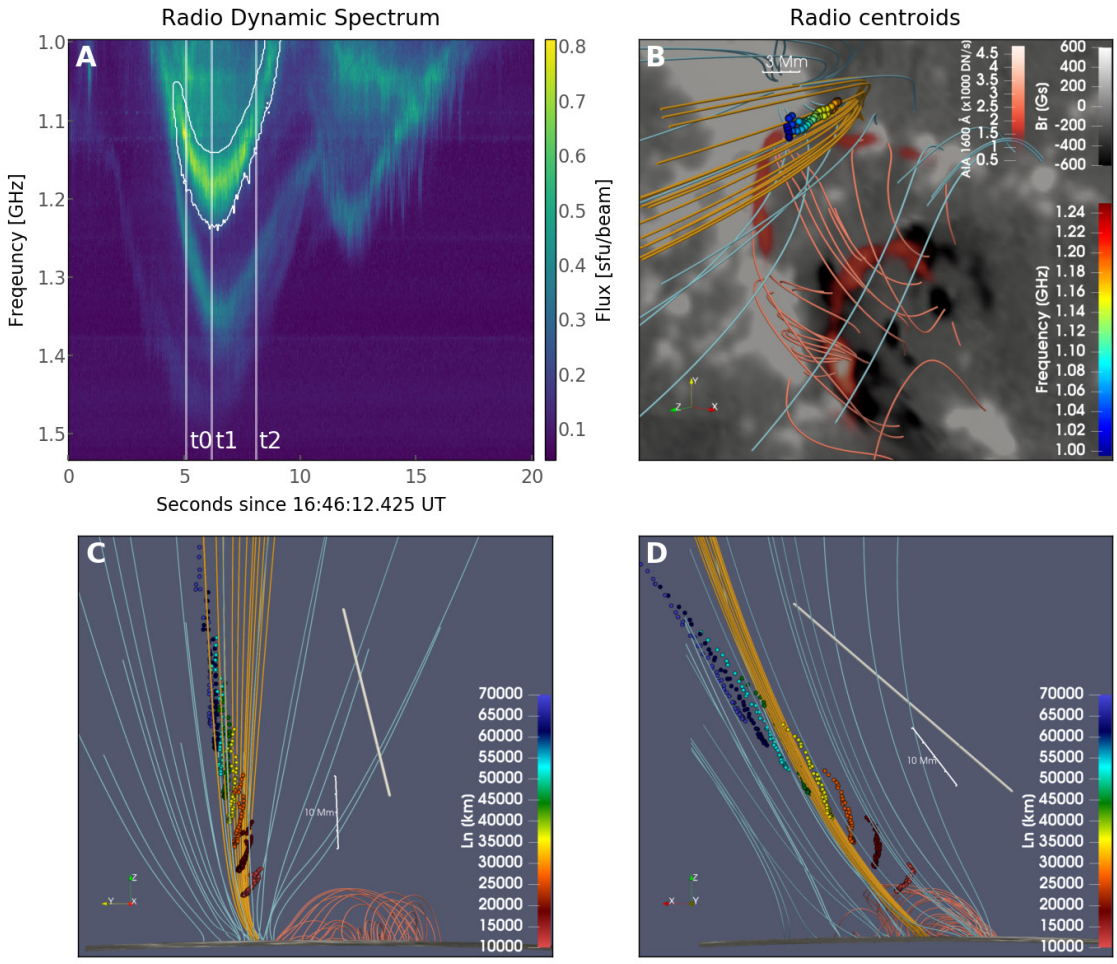


**Figure 7.** Three-dimensional locations of the radio burst centroids for emission lane L1 in Burst 2 (as denoted in Figure 5(F)). (A) Dynamic spectrum of the Burst 2. All the frequency-time pixels on emission lane L1 selected for dynamic spectroscopic imaging are enclosed by solid white curves. (B) Burst centroid locations of the selected frequency-time pixels of L1. Each centroid represents the average location of all frequency pixels across the emission lane at a given time, colored in their mean frequency (frequency increases from blue to red). Colored curves are selected magnetic field lines from the potential field extrapolation model based on the SDO/HMI line-of-sight photospheric magnetogram observed at around 17:00 UT (grayscale background). Field lines with pink color denote closed field associated with the reconnected loops, while those with yellow (cyan) color denote open field lines that connect to the northern ribbon (sunspot). The double flare ribbons seen in AIA 1600 Å are shown in red. The FOV is indicated by the dashed box in Figure 5(C) and (D). (C) Three-dimensional distribution of the radio centroids assuming different density scale heights $L_n$, viewing from the east side of the active region. Each set of centroids in the same color represents the 3D projection of all the centroids shown in (B) by assuming a given value of $L_n$. The thick white line indicates the LOS of an Earth-based observer. (D) same as (C), but viewed from the north side of the active region.

Figure 8(A) shows the same distribution of radio centroids derived from emission lane L1 as in Figure 7(B), but instead colored in time. It displays an evident motion in projection: The radio source first moves toward the flare ribbon as frequency increases (blue to red color in Figure 7(B) and blue to white color in Figure 8(B)) until it reaches the maximum frequency at the lowest height, and then bounces back to the opposite direction away from the ribbon as frequency decreases (red to blue color in Figure 7(B) and white to red color in Figure 8(B)). The average speed in projection is ∼1000–2000 km $s^{-1}$, which is typical for propagating Alfvén or fast-mode magnetosonic waves in the low corona (e.g., Nitta et al. 2013; Liu et al. 2018).This is a strong indication for the radio emission being associated with a propagating Alfvén or fast-mode MHD disturbance in a magnetic tube in the close vicinity of the flare ribbon. As discussed in Section 2.1, the presence of ubiquitous MHD disturbances in the flaring region is strongly implicated by the observation of large-scale, fast PDs observed by SDO/AIA at about the same time.

### 2.3. *Radio source motion in 3D*

In order to place the location of the radio centroids into the physical context of the flare, we perform potential field extrapolation based on the SDO/HMI line-of-sight photospheric data right after the flare peak at 17:00 UT (Bobra et al. 2014; Hoeksema et al. 2014) to derive the coronal magnetic field. Selected magnetic field lines from the extrapolation results are shown in Figure 7(B) for regions around the location of the radio burst centroids and the postflare arcades. It is shown that the spatial distribution of the radio centroid position at different frequencies tends to follow the magnetic field lines (yellow color) rooted around the northern flare ribbon, with its higher-frequency end located closer to the ribbon: This is consistent with the expectation for plasma radiation, in which a higher emission frequency is emitted in regions with higher plasma density that are typically located at lower coronal heights ($\nu \approx s\nu_{pe} \approx 8980s\sqrt{n_e}$ Hz, where $s$ is the harmonic number, $\nu_{pe}$ is the electron plasma frequency, and $n_e$ is the local electron density in $cm^{-3}$).

Since the emission is highly polarized, it is reasonable to assume fundamental plasma radiation as the responsible emission mechanism (i.e., harmonic number $s$=1 and $\nu \approx \nu_{pe}$). In this case, the emission frequency $\nu$ of the radio source centriod $I_{\rm pk}(\theta, \phi, \nu, t)$ can be directly translated into the plasma density of the source $n_e$. By further assuming a coronal density model $n_e(h)$ where $h$ is the coronal height, we can thus map the measured centroid locations in 2D projection to three dimensional (3D) locations in the corona, i.e., from $I_{\rm pk}(\theta, \phi, \nu, t)$ to $I_{\rm pk}(\theta, \phi, h, t)$. Similar practice has been used in Aurass et al. (2005) and more recently, Wang et al. (2017), for deriving 3D trajectories of dm-$\lambda$ fiber bursts in the corona. Here we adopt a barometric density model with an exponential form

$$n_{\rm e}(h) = n_{e0} \exp\left(-\frac{h - h_0}{L_n}\right) \tag{2}$$

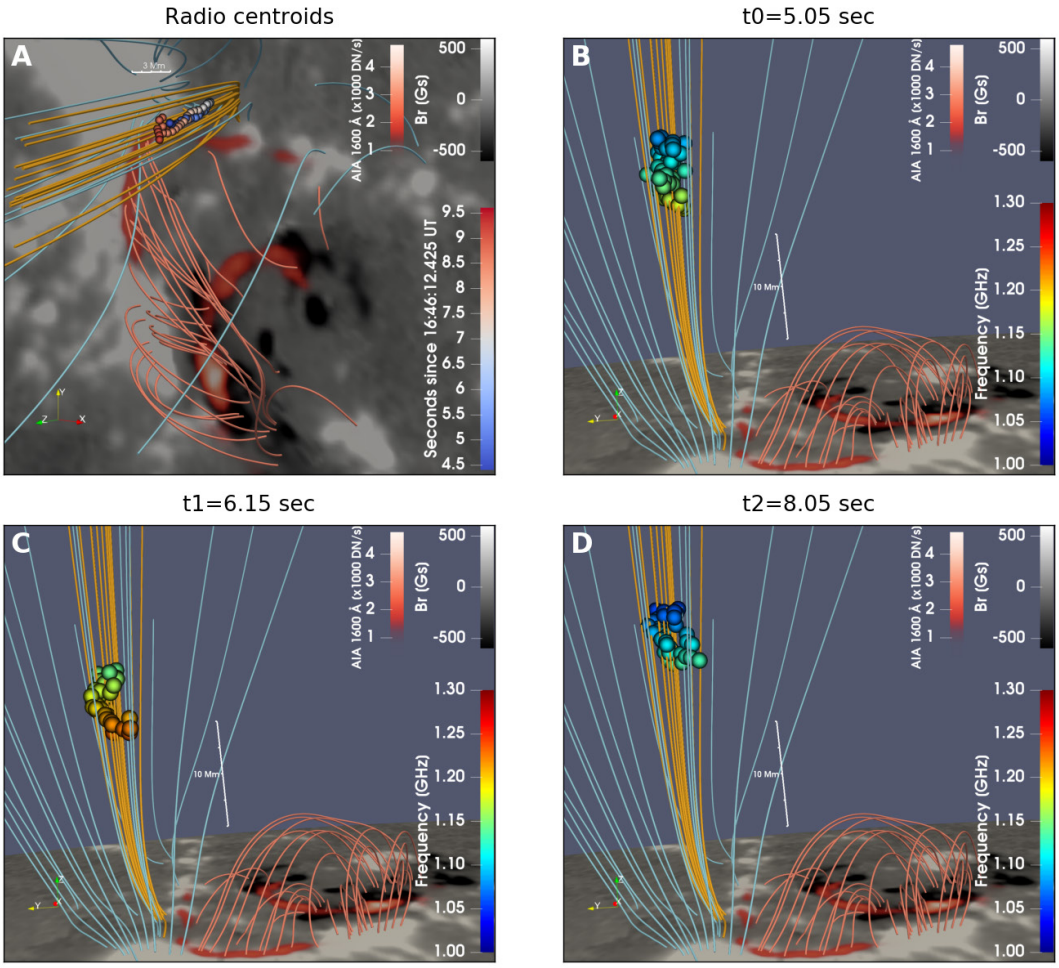


**Figure 8.** (A) Similar as Figure 7, but the centroids are colored from blue to red in time. (B-D) Emission centroids of L1 in three dimensional view at three 100 ms integrations (denoted as t0, t1 and t2 in Figure 7(A)). The centroids and contours are colored from blue to red in increasing frequency. (An animation of this figure is available in the online journal.)

where $h$ is the height above the solar surface, $L_n$ is the density scale height, and $n_{e0}$ is the density at a reference height $h_0$. Such a density model describes the density variation for an isothermal, plane-parallel atmosphere under hydrostatic equilibrium (e.g., Aschwanden 2005), and has been widely used in the literature as a zero-order approximation for estimating the coronal heights of various solar coherent radio bursts (e.g., Aurass et al. 2005; Chen et al. 2011, 2013; Wang et al. 2017). For simplicity we fix the parameters $n_{e0}$ and $h_0$ to be $\sim 3 \times 10^{10}$ cm$^{-3}$ and ~2000 km at the top of the chromosphere according to the VAL model (Vernazza et al. 1981), and investigate the effect of different choices of $L_n$ on the resulted 3D distribution of the radio source centroids.

Figures 7(C) and (D) demonstrate the inferred 3D distributions of the radio source centroids with different choices of $L_n$ from 10 Mm to 70 Mm, viewing from the eastern and northern side of the AR respectively. Each set of the 3D centroid positions at a

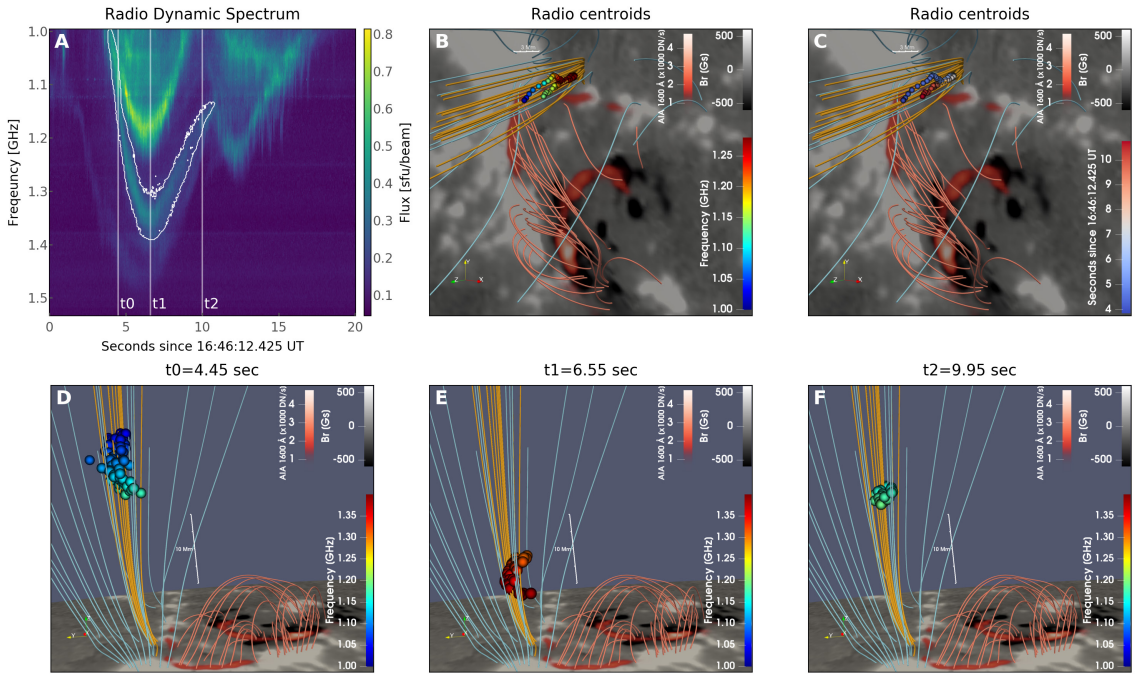


**Figure 9.** (A-B) Same as Figure 7(A-B) but for the emission lane L2 of Burst 2. (C-F) Same as Figure 8(A-D) but for the emission lane L2 of Burst 2. (An animation of this figure is available in the online journal.)

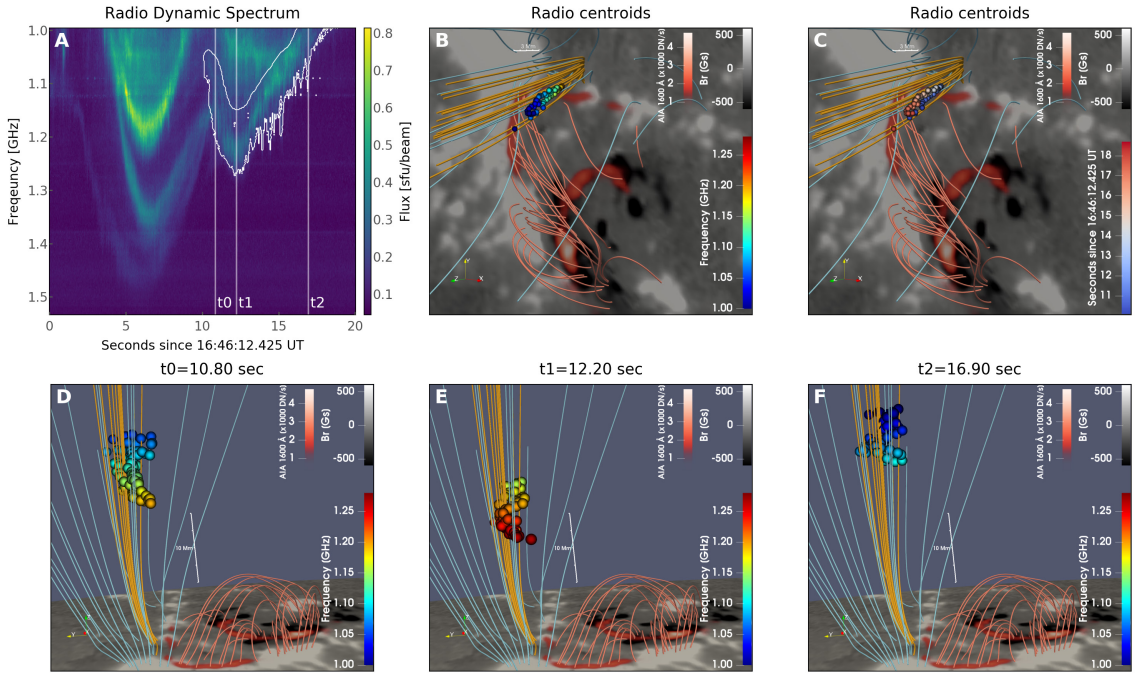


**Figure 10.** Same as Figure 9, but for the emission lane L3 of Burst 2. (An animation of this figure is available in the online journal.)

given $L_n$ is shown as dots with the same color (from red to blue in increasing $L_n$). It is obvious from the figure that the choice of a greater value of $L_n$ yields a more stretched distribution of the radio centroids in height, and *vice versa*. Such a proportionality between the vertical extent $h_{\rm tot}$ of the radio sources and $L_n$ is straightforward to find if we combine the barometric density model (Eq. 2) with the frequency-density relation for plasma radiation $\nu \propto \sqrt{n_e}$, which gives $h_{\rm tot} \approx 2L_n\Delta\nu_{\rm tot}/\nu$, where $\Delta\nu_{\rm tot}$ is the total frequency width of the radio burst determined from the dynamic spectrum. More importantly, different choices of $L_n$ affect how the radio source centroids are distributed with regard to the extrapolated magnetic field lines in 3D: For small $L_n$ values, the centroids tend to distribute across the field lines within a small range of vertical heights, while for $L_n$ values in the intermediate range (∼35–50 Mm), the spatial extension of the centroids tend to agree with the direction of the extrapolated field lines. As discussed earlier, the temporal evolution of radio source (1000–2000 km $s^{-1}$ in projection) is consistent with a physical motion of the emission source at Alfvénic or fast-mode magnetosonic speed. Because the radio source appears to be closely associated with the flare ribbon both spatially and temporally (c.f., Section 2.1), we assume that the radio source moves along (or within a small angle with regard to) the reconnected magnetic loops that link to the flare ribbon. In this case, the corresponding $L_n$ values fall into the ∼35–50 Mm range. For subsequent discussions, we will adopt $L_n = 40$ Mm, with the understanding that this parameter is not very well determined due to the inherent limitations of magnetic field extrapolation, the uncertainty on the exact direction of propagation of the radio source in 3D, and may vary from burst to burst.

Figure 8(B)–(D) shows the inferred 3D spatial and temporal evolution of the radio centroids of emission lane L1 after adopting the coronal density model with $L_n = 40$ Mm, viewing from the east side of the AR. It is clear that the radio source first moves downward along a converging magnetic field tube (panels B and C) and then bounces backward after it reaches the lowest altitude (or highest frequency). We also extend the same analysis to emission lanes L2 and L3 of Burst 2. The results show a similar spatiotemporal evolution of the radio source centroids as lane L1 (Figures 9 and 10). We caution that the absolute height of the radio source as well as the point of reflection, however, depends strongly on the selection of parameters in the coronal density and magnetic field model adopted here, which may very well be different for radio bursts propagating along different flare loops. Therefore, the 3D source evolution shown in Figures 8–10 should only be considered as a qualitative representation.

## 3. DISCUSSIONS

We briefly summarize the observational results in the previous section as follows:

1. The radio bursts of interest appeared during the late impulsive phase of a C7.2 two-ribbon solar flare that associated with a failed filament eruption, when

large-scale, fast-propagating EUV disturbances were observed throughout the flare region.

2. The location of the radio source coincides with the northern flare ribbon and HXR footpoints. In addition, the radio source appears to show close spatial and temporal association with transient (E)UV brightenings on the ribbon.

3. The bursts have a high brightness temperature of $> 10^7$ K and is completely polarized in the sense of *o* mode.

4. The bursts consist of multiple emission lanes that exhibit a low-high-low frequency drift pattern in the radio dynamic spectrum with a moderate relative frequency drift rate of $\dot{\nu}/\nu \lesssim 0.2\mathrm{s}^{-1}$, which is typical for intermediate drift bursts in the dm-$\lambda$ wavelength range.

5. Imaging at all time and frequency pixels where the bursts are present shows that the radio source propagates at a speed of 1–2 Mm $\mathrm{s}^{-1}$ in projection. The low-high-low frequency drift pattern corresponds to the source firstly moving downward along the flaring loop before it reaching the lowest point and bouncing back upward.

6. Some of the emission lanes consist of multitudes of subsecond-period oscillations in emission frequency with an amplitude of $\delta\nu/\nu \approx$1–2%.

What is the nature of the propagating radio source that reflects at or near the flare ribbon? First, they are most likely associated with fundamental plasma radiation, which is due to the nonlinear conversion from plasma Langmuir waves induced by the presence of nonthermal electrons. This is because that the bursts have narrow frequency bandwidth ($\delta\nu/\nu \approx 6\%$) and fast temporal varying features, and are nearly 100% polarized. Second, the propagation speed of the emission source (1–2 Mm $\mathrm{s}^{-1}$ in projection) is too slow for type-III-burst-emitting electron beams (which usually propagate at 0.1–0.5$c$, see, e.g., Chen et al. 2013; McCauley et al. 2017; Chen et al. 2018a), but likely too fast for slow-mode magnetosonic waves, unless the temperature in the source reaches over ∼50 MK. The most probable candidate for the radio-emission-carrying disturbance is thus Alfvénic or fast-mode magnetosonic waves, which propagate at ∼1–4 Mm $\mathrm{s}^{-1}$ under typical coronal conditions. The Alfvénic or fast-mode waves can be excited by a broadband driver, such as the impulsive flare energy release, and propagate outward from the energy release site. For fast-mode waves to achieve focused, field-aligned energy transport, an overdense magnetic tube would be required to act as a waveguide (Roberts et al. 1983, 1984; Nakariakov et al. 2004; Russell & Stackhouse 2013; Kolotkov et al. 2018), which, in our case, can be the freshly reconnected flaring loops that connect to the flare ribbons. The observed reflection of the waves at or near the flare ribbon may be due to sharp gradients at and/or below the transition region (Emslie & Sturrock 1982; Fletcher & Hudson 2008; Russell

& Stackhouse 2013; Russell & Fletcher 2013; Reep et al. 2018). It is, however, less clear from our observations regarding the physical connection between the nonthermal electrons (responsible for the production of Langmuir waves) and the MHD waves: The energetic electrons could be accelerated locally within the waves by a variety of means including acceleration by parallel electric field, turbulence, or a first-order Fermi process with the wavefront acting as a moving mirror (c.f., Fletcher & Hudson 2008), or originated from an acceleration site elsewhere (e.g., at the reconnection site or flare looptop) but trapped with the propagating MHD waves.

It is particularly intriguing that some of the emission lanes show fast, subsecond-scale quasi-periodic oscillations in the emission frequency with an amplitude of $\delta\nu/\nu \approx$1–2%. Under the plasma radiation scenario, $\delta\nu/\nu$ can be directly translated into small density perturbations of $\delta n_e/n_e \approx 2\delta\nu/\nu \approx$2–4%. If these small-amplitude oscillations in frequency can be interpreted as weak density perturbations associated with the propagating waves, the fast-mode magnetosonic mode scenario would be more probable, as pure Alfv́en modes are incompressible. We note that such small density disturbances are hardly detectable by current EUV or SXR imaging instrumentation, mainly because that the resulted small fluctuation level in the EUV/SXR intensity $\delta I/I \lesssim 2\delta n_e/n_e \approx 4\%$ (Cooper et al. 2003) is very difficult to detect against the background. In addition, the subsecond periodicity of the density perturbations is at least an order of magnitude below the time cadence of the current EUV/SXR imaging instrumentation (e.g., 12 s for SDO/AIA). We note that, however, subsecond-scale oscillations in the solar corona have been reported in the literature based on non-imaging radio or X-ray light curves or dynamic spectra during flares (e.g., Rosenberg 1970; Bogovalov et al. 1983; Fu et al. 1990; Qin et al. 1996; Chen & Yan 2007; Tan et al. 2010; Yu et al. 2013). Aschwanden (1987) summarized the possible mechanisms into three categories: 1) quasi-periodic injections of nonthermal electrons, 2) fast cyclic self-organizing systems of plasma instabilities associated with the wave-particle or wave-wave interaction processes, and 3) MHD oscillations. While we cannot completely rule out the other possibilities, the observed oscillations in radio emission frequency (or plasma density), combined with the fast-moving radio source with a speed characteristic of Alfvénic or fast-mode waves are strong indication of a weakly compressible, propagating MHD wave packets in the flaring loops that cause localized quasi-periodic modulations of the plasma density along its way.

The spatial scale of the radio-emitting fast wave packages can be inferred from the instantaneous frequency bandwidth $\Delta\nu/\nu$ of individual emission lanes based on the plasma radiation scenario: $\Delta L = 2L_n(\Delta\nu/\nu)$, where $L_n = n_e/(dn_e/dl)$ is the density scale height. For a magnetic loop under hydrostatic equilibrium, the density gradient is along the vertical direction $z$, and the density scale height is $L_n = n_e/(dn_e/dl) = 2k_BT/(\mu m_H g) \approx 46T_{\rm MK}$ Mm, where $g$ is the gravitational acceleration near the solar surface, $m_H$ is the mass of the hydrogen atom, $T_{\rm MK}$ is the coronal temperature in million Kelvin, and $\mu \approx 1.27$ is the mean molecular weight for

typical coronal conditions (Aschwanden 2005). In this case, a frequency bandwidth of $\Delta\nu/\nu \approx 6\%$ implies a vertical extent of the source of $\Delta L_z \approx 5.5 T_{\rm MK}$ Mm. Such an estimate of the source size is not inconsistent with the small, few-Mm-scale distribution of the radio source centroids across all frequencies on the emission lane at a given time in the plane of the sky $\Delta L_{\parallel}$, although the latter is complicated by the scattering of the radio waves due to coronal inhomogeneities (c.f., discussions in Section 2.2). It is interesting to note that this size estimation is about an order of magnitude smaller than the apparent size of each radio image (with a half-power-full-maximum size of ∼30–50 Mm; cf. Figure 5(D)). Such an extended radio image can be likely attributed to the angular broadening of the radio source caused by random scattering of the radio waves traversing the inhomogeneous corona (Bastian 1994). Indeed, Bastian (1994) estimated an angular broadening of a few tens of arcseconds at our observing frequency and source longitude, which is at the same order of magnitude as our apparent source size.

The wavelength associated with the subsecond-period oscillations can be estimated via $\lambda \approx v_{\rm p} P$, where $v_{\rm p}$ is the phase speed of the waves, taken to be at the same order of magnitude as the observed wave speed ∼3 Mm s$^{-1}$ (after assuming an inclination angle of 60° inferred from the magnetic field extrapolation, cf. Section 2.3) that presumably represents the group speed of the wave packet $v_{\rm g}$ (see, e.g., Roberts et al. 1984 for discussions regarding the relation between $v_{\rm p}$ and $v_{\rm g}$), and $P$ is the wave period, taken to be ∼0.5 s from the observed periods of the density fluctuations (c.f., Figure 6). Therefore, the wavelength of the oscillations is estimated as $\lambda \approx 1.5$ Mm, much smaller than the size of the propagating radio source ($\Delta L > \Delta L_z \approx 5.5 T_{\rm MK}$ Mm). We therefore argue that each radio source is likely a propagating MHD wave packet that consists of multiple short-period oscillations.

During each burst period, multiple emission lanes are present in the radio dynamic spectrum with almost synchronous frequency drift behavior (which is particularly clear for Burst 2; cf. Figure 5(I)). Imaging results of the different emission lanes suggest that they are all located at the same site and share very similar spatiotemporal behavior in projection, but show subtitle differences (cf. Figures 8(A), 9(C), and 10(C)). Their different emission frequencies, however, imply that the corresponding propagating disturbances have different plasma densities. Some other types of solar dm-$\lambda$ bursts, in particular, zebra-pattern bursts (ZBs), also display multiple emission lanes. One leading theory for ZBs attributes the observed multiple lanes to radio emission at the plasma upper-hybrid frequency $\nu_{\rm uh}$ that coincides with harmonics of the electron gyrofrequency $\nu_{\rm ce}$, i.e., $\nu \approx \nu_{\rm uh} \approx (\nu_{\rm pe}^2 + \nu_{\rm ce}^2)^{1/2} \approx s\nu_{\rm ce}$ (Winglee & Dulk 1986; Zlotnik et al. 2003; Kuznetsov & Tsap 2007; Chen et al. 2011; Zlotnik 2013; Karlický & Yasnov 2018). However, unlike the ZBs, the frequency spacing between different emission lanes in this burst is irregular and varies in time. Moreover, although the frequency turnover time of different emission lanes $t_{\rm o}$ is very close to each other, it differs by ∼0.5–0.8 s (red arrows in Figure 5(G) and (I)) and does not show

a systematic lag in frequency as is usually present in ZBs (Kuznetsov & Tsap 2007; Chen & Yan 2007; Yu et al. 2013). Therefore, we argue that the different emission lanes are not due to harmonics of a particular plasma wave mode. Instead, they are related to different wave packets, which are triggered by the same impulsive energy release event, propagating in magnetic flux tubes with different plasma properties.

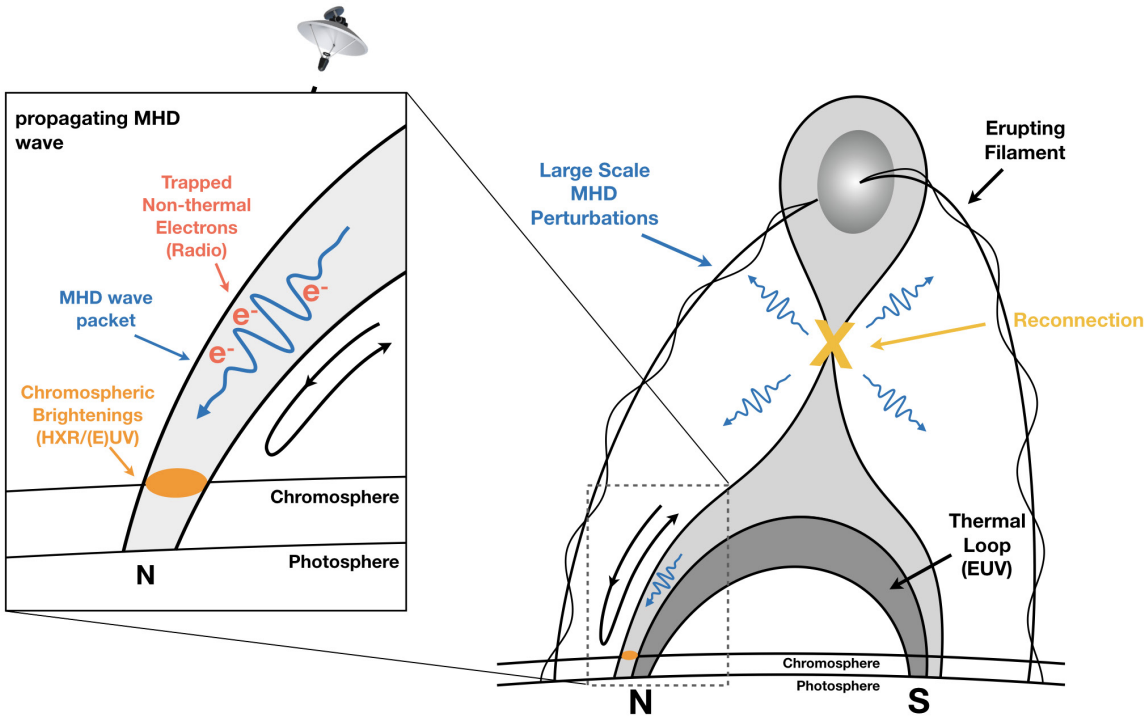


**Figure 11.** Schematic illustration of the observed radio bursts of interest. The impulsive energy release associated with the filament eruption and the two-ribbon flare generates ubiquitous MHD disturbances, some of which propagate along newly reconnected field lines in the form of MHD wave packets that contain multiple subsecond-period oscillations. Electrons trapped or accelerated within these wave packets generate Langmuir waves and convert to radio emission. Some of the wave packets can reflect at or near the flare ribbon due to sharp gradients, resulting in the observed spatial motion of the radio source and the low-high-low frequency drift pattern of the radio burst in the dynamic spectrum. The (E)UV brightenings at the flare ribbon may be associated with heating by the precipitated energetic electrons or the deposited wave energy.

The schematic in Figure 11 summarizes our interpretation of the observed radio bursts in terms of propagating MHD wave packets that contain multiple subsecond-period oscillations within the context of the filament eruption and two-ribbon flare. As introduced in Section 1, subsecond-period MHD waves may be a viable mechanism responsible for transporting a substantial amount of the magnetic energy released in the corona downward to the lower atmosphere, resulting in intense plasma heating and/or particle acceleration. Let us consider the scenario of fast-mode MHD waves guided by dense magnetic flux tubes as an example (Edwin & Roberts 1983; Cooper et al. 2003). The kinetic energy flux associated with propagating MHD waves can be

estimated as $F_K \approx \frac{1}{2}\rho\delta v^2 v_g$ (Tomczyk et al. 2007; Van Doorsselaere et al. 2014), where $\rho \approx m_H n_e$ is the mass density, $\delta v$ is the amplitude of the velocity perturbation, and $v_g$ is the group speed of the propagating MHD wave. Estimates for both $\rho$ and $v_g$ can be conveniently obtained from our observations of the radio emission frequency and the radio source motion. Although the velocity perturbation $\delta v$ is not directly measured by our observations, it is intimately related to the observed density perturbation amplitude $\delta\rho \approx m_H \delta n_e$ through the continuity equation in the small perturbation regime:

$$\frac{d(\delta\rho)}{dt} = -\rho_0 \nabla \cdot \delta v, \tag{3}$$

It is beyond the scope of the current study to examine the detailed relation for all possible wave modes propagating in coronal loops with different density profiles. Nevertheless, under typical coronal conditions, it has been shown by previous studies that $\delta v/v_g$ is at the same order of magnitude as $\delta n_e/n_e$ for fast-mode MHD waves propagating along dense coronal loops (Cooper et al. 2003; Van Doorsselaere et al. 2008). The latter is found to be $\delta n_e/n_e \approx 2\delta\nu/\nu \approx$2–4%. Following these assumptions, we estimate the energy flux as 2–8$\times10^8$ erg s$^{-1}$ cm$^{-2}$, with $n_e \approx 2\times10^{10}$ cm$^{-3}$, $\delta v/v_g \approx$2–4%, and $v_g \approx 3$ Mm s$^{-1}$.

Is the estimated energy flux carried by the MHD disturbances energetically important in this flare? The energy flux required to power flares can be inferred using a variety of observational diagnostic methods including broadband imaging of flare ribbons in white light and UV (Fletcher et al. 2007; Qiu et al. 2012; Liu et al. 2013), as well as HXR spectroscopic and imaging observations of flare footpoints (Fletcher et al. 2007). Here we adopt the method developed by Qiu et al. (2012) to estimate the energy flux needed to account for flare heating based on SDO/AIA 1600 Å UV observations of the flare ribbons. The energy flux $F_i(t)$ of flare heating is related to UV 1600 Å ribbon brightening at pixel $i$ as

$$F_i(t) = \lambda I_i^{\rm pk} \exp\left[-\frac{(t-t_i^{\rm pk})^2}{2\tau_i^2}\right] \text{ erg s}^{-1}\text{ cm}^{-2}, \tag{4}$$

where the exponential term is the Gaussian function used to fit the rise phase of the UV count rate light curve that has a characteristic rise time $\tau_i$ and peaks at $t_i^{\rm pk}$, and $\lambda$ is the scaling factor that converts the observed peak UV count rate $I_i^{\rm pk}$ at pixel $i$ (in DN s$^{-1}$ pixel$^{-1}$) to the estimated energy flux responsible for the flare heating (erg s$^{-1}$ cm$^{-2}$), which depends on not only the mechanism of UV radiation upon heating in the lower atmosphere, but also the instrument response. Qiu et al. (2012) and Liu et al. (2013) performed detailed loop heating modeling studies of two flares, and found that $\lambda$ generally lies in 2–3$\times10^5$ erg DN$^{-1}$ pixel/cm$^{-2}$ to best match the model-computed GOES SXR light curves with the observations. Here we take $\lambda \approx 2.7\times10^5$ erg DN$^{-1}$ pixel/cm$^{-2}$ quoted in Qiu et al. (2012) for our order of magnitude estimate. We have traced all pixels in AIA 1600 Å UV images that

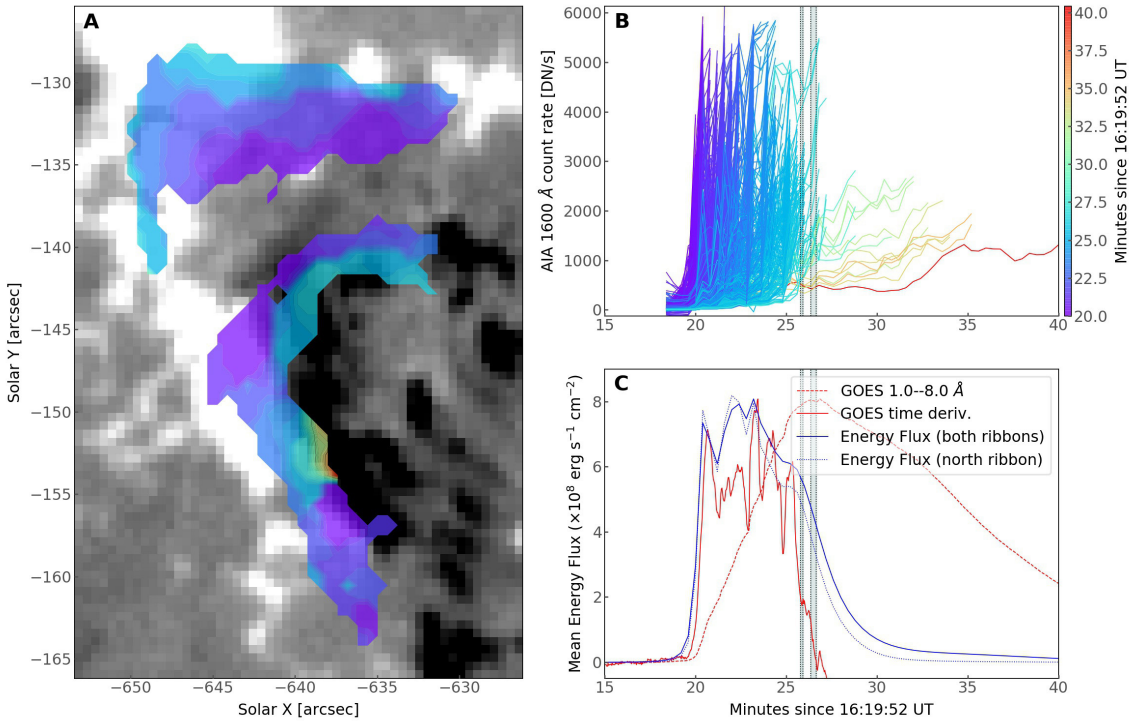


**Figure 12.** UV observations of the flare ribbons and the associated energy flux. (A) Temporal evolution of the double UV flare ribbons in SDO/AIA 1600 Å, colored from purple to red in time, overlaid on SDO/HMI longitudinal magnetogram at 16:46:13 UT (grayscale background). (B) SDO/AIA 1600 Å light curves of all pixels on the flare ribbons (within the colored areas in (A); only the ascending part is shown). (C) GOES 1–8 Å light curve (red dashed) and its time derivative (red). Also shown is the evolution of the energy flux of flare heating inferred from the observed UV 1600 Å flare ribbon emission, averaged over both ribbons (blue) and north ribbon only (blue dashed). The times of the two radio bursts in Figure 1(A) are demarcated with vertical lines in panels (B) and (C).

show flare ribbon brightenings, showing in Figure 12(A) colored in their peak time $t_i^{\rm pk}$ from purple to red. The flare ribbons show an evident separation motion during the impulsive phase of the flare, which is characteristic of two-ribbon flares and has been considered as one of the primary evidence for magnetic-reconnection-driven flare energy release (Qiu et al. 2002). The corresponding UV count rate light curves for all ribbon pixels are shown in Figure 12(B), again colored in their peak time (only the rising portion of the light curve is shown). The UV ribbon brightenings agree very well in time with the GOES SXR derivative (thick red curve in Figure 12(C)), suggesting that heating of the flare loops is mainly driven by the "evaporation" of the heated chromospheric plasma. The estimated energy flux averaged over all ribbon pixels $\overline{F}(t)$ based on Eq. 12 is shown as the blue curve in Figure 12(C). Also shown is the average $\overline{F}(t)$ estimated using only pixels of the northern ribbon (dashed blue curve), with which the radio bursts appear to associate temporally and spatially (c.f., Figure 3). The values are in the range of $10^8$–$10^9$ erg s$^{-1}$ cm$^{-2}$, which are typical for GOES C-class flares. At the time of the radio burst, the average $\overline{F}(t)$ at the northern

ribbon is about $4 \times 10^8$ erg s$^{-1}$ cm$^{-2}$, which is comparable to the estimated energy flux carried by the observed subsecond-period MHD wave packets.

We note that, however, such coherent-burst-emitting waves can only be observed when the following conditions are met: 1) Flare-accelerated electrons are present in the vicinity of the MHD waves. 2) Conditions are satisfied for inducing nonlinear growth of Langmuir waves and the subsequent conversion to transverse radio waves. 3) The radio waves are emitted within the bandwidth of the instrument (1–2 GHz in our case). 4) The instrument is sensitive enough to distinguish the radio bursts from the background active region and flare emission—the flux density of the bursts is only $\sim 1$ sfu (1 sfu = $10^4$ Jansky) in our case, which is barely above the noise level of most non-imaging solar radio spectrometers. For these reasons, the radio bursts appear relatively rare, thereby their volume filling factor in the entire flaring region is essentially unknown. Moreover, although possible signatures of wave damping seem to present in some bursts that we observe (c.f., Figure 6(B–E)), which may be due to energy loss during their propagation, the fraction of total energy deposited to the lower solar atmosphere from the waves remains undetermined in this study. However, considering the presence of ubiquitous large-scale fast EUV waves throughout the active region around the same time, it is reasonable to postulate that these short-period waves are also ubiquitously present in the flaring region. If this is the case, these waves may play a role in transporting the released flare energy during the late impulsive phase of this flare, likely alongside the accelerated electrons, and the subsequent heating of the flare ribbons and arcades.

## 4. CONCLUSION

Here we report radio imaging of propagating MHD waves along post-reconnection flare loops during the late impulsive phase of a two-ribbon flare. This is based on observations of a peculiar type of dm-$\lambda$ radio bursts recorded by the VLA. In the radio dynamic spectrum, the bursts show a low-high-low frequency drift pattern with a moderate frequency drift rate of $\dot{\nu}/\nu \lesssim 0.2$. VLA's unique capability of imaging with spectrometer-like temporal and spectral resolution (50 ms and 2 MHz) allows us to image the radio source at every pixel in the dynamic spectrum where the burst is present. In accordance with its low-high-low frequency drift behavior, we find that the radio source firstly moves downward toward a flare ribbon before it reaches the lowest height and turns upward. The measured speed in projection is $\sim$1–2 Mm/s, which is characteristic of Alfvénic or fast-mode MHD waves in the low corona. Furthermore, we find that the bursts consist of many sub-second, quasi-periodic oscillations in emission frequency, interpreted as fast oscillations within propagating MHD wave packets. As illustrated in Figure 11, these wave packets are likely triggered by the impulsive flare energy release, and subsequently propagate downward along the newly reconnected field lines down to the flare ribbons. From the observed density oscillations and the source motion, we estimate that these wave packets carry an energy

flux of 2–8$\times10^8$ erg s$^{-1}$ cm$^{-2}$, which is comparable to the average energy flux required for driving the flare heating during the late impulsive phase of the flare estimated from the UV ribbon brightenings. In addition, the radio source seems to show a close spatial and temporal association with the transient brightenings on the flare ribbon. As introduced in Section 1, such subsecond-period MHD waves have long been postulated as an alternative or complementary means for transporting the bulk of energy released in flares alongside electron beams, resulting in strong plasma heating and/or particle acceleration. Here we provide, to the best of our knowledge, the first possible observational evidence for these subsecond-period MHD waves propagating in post-reconnection magnetic loops derived from imaging and spectroscopy data, and demonstrate their possible role in driving plasma heating during the late impulsive phase of this flare event. Future studies are required to, first of all, investigate their presence in other flare events, and moreover, establish whether or not they are energetically important in transporting the released flare energy during different flare phases.

We thank Sophie Musset for her help in producing the RHESSI X-ray image. We also thank Tim Bastian, John Wygant, Lindsay Glesener, Kathy Reeves, and Dale Gary for helpful discussions, as well as an anonymous referee who provided constructive comments to improve the paper. The National Radio Astronomy Observatory is a facility of the National Science Foundation (NSF) operated under cooperative agreement by Associated Universities, Inc. This work made use of open-source software packages including CASA (McMullin et al. 2007), SunPy (SunPy Community et al. 2015), and Astropy (Astropy Collaboration et al. 2013, 2018). BC and SY are supported by NASA grant NNX17AB82G and NSF grant AGS-1654382 to the New Jersey Institute of Technology.

*Facilities:* VLA, SDO, RHESSI, GOES

## REFERENCES

Alaoui, M., & Holman, G. D. 2017, ApJ, 851, 78

Aschwanden, M. J. 1987, SoPh, 111, 113

—. 2005, Physics of the Solar Corona. An Introduction with Problems and Solutions (2nd edition)

Aschwanden, M. J., Brown, J. C., & Kontar, E. P. 2002, SoPh, 210, 383

Astropy Collaboration, Robitaille, T. P., Tollerud, E. J., et al. 2013, A&A, 558, A33

Astropy Collaboration, Price-Whelan, A. M., Sipőcz, B. M., et al. 2018, AJ, 156, 123

Aurass, H., Rausche, G., Mann, G., & Hofmann, A. 2005, A&A, 435, 1137

Bárta, M., & Karlický, M. 2005, ApJ, 631, 612

Bastian, T. S. 1994, ApJ, 426, 774

Battaglia, M., Fletcher, L., & Benz, A. O. 2009, A&A, 498, 891

Battaglia, M., & Kontar, E. P. 2011, A&A, 533, L2

Benz, A. O. 2017, Living Reviews in Solar Physics, 14, 2
Benz, A. O., & Mann, G. 1998, A&A, 333, 1034
Bobra, M. G., Sun, X., Hoeksema, J. T., et al. 2014, SoPh, 289, 3549
Bogovalov, S. V., Iyudin, A. F., Kotov, Y. D., et al. 1983, Soviet Astronomy Letters, 9, 163
Brannon, S. R., Longcope, D. W., & Qiu, J. 2015, ApJ, 810, 4
Brown, J. C. 1971, SoPh, 18, 489
Brown, J. C., Aschwanden, M. J., & Kontar, E. P. 2002, SoPh, 210, 373
Brown, J. C., Turkmani, R., Kontar, E. P., MacKinnon, A. L., & Vlahos, L. 2009, A&A, 508, 993
Carmichael, H. 1964, A Process for Flares, 451
Chen, B., Bastian, T. S., & Gary, D. E. 2014, ApJ, 794, 149
Chen, B., Bastian, T. S., Gary, D. E., & Jing, J. 2011, ApJ, 736, 64
Chen, B., Bastian, T. S., Shen, C., et al. 2015, Science, 350, 1238
Chen, B., Bastian, T. S., White, S. M., et al. 2013, ApJ, 763, L21
Chen, B., & Yan, Y. 2007, SoPh, 246, 431
Chen, B., Yu, S., Battaglia, M., et al. 2018a, ApJ, 866, 62
Chen, X., Kontar, E. P., Yu, S., et al. 2018b, ApJ, 856, 73
Condon, J. J. 1997, Publications of the Astronomical Society of the Pacific, 109, 166
Cooper, F. C., Nakariakov, V. M., & Williams, D. R. 2003, A&A, 409, 325
Edwin, P. M., & Roberts, B. 1983, SoPh, 88, 179
Emslie, A. G. 1980, ApJ, 235, 1055
Emslie, A. G., Dennis, B. R., Holman, G. D., & Hudson, H. S. 2005, Journal of Geophysical Research (Space Physics), 110, A11103
Emslie, A. G., & Sturrock, P. A. 1982, SoPh, 80, 99
Emslie, A. G., Kucharek, H., Dennis, B. R., et al. 2004, Journal of Geophysical Research (Space Physics), 109, A10104
Emslie, A. G., Dennis, B. R., Shih, A. Y., et al. 2012, ApJ, 759, 71
Fletcher, L., Hannah, I. G., Hudson, H. S., & Metcalf, T. R. 2007, ApJ, 656, 1187
Fletcher, L., & Hudson, H. S. 2008, ApJ, 675, 1645
Fu, Q.-J., Gong, Y.-F., Jin, S.-Z., & Zhao, R.-Y. 1990, SoPh, 130, 161
Hammer, D. A., & Rostoker, N. 1970, Physics of Fluids, 13, 1831
Hirayama, T. 1974, SoPh, 34, 323
Hoeksema, J. T., Liu, Y., Hayashi, K., et al. 2014, SoPh, 289, 3483
Holman, G. D. 2012, ApJ, 745, 52
Hoyng, P., Brown, J. C., & van Beek, H. F. 1976, SoPh, 48, 197
Huang, J., & Tan, B. 2012, ApJ, 745, 186
Karlický, M., Bárta, M., Jiřička, K., et al. 2001, A&A, 375, 638
Karlický, M., Mészárosová, H., & Jelínek, P. 2013, A&A, 550, A1
Karlický, M., & Yasnov, L. 2018, A&A, 618, A60
Keiling, A., Wygant, J. R., Cattell, C., et al. 2000, Geophysical Research Letters, 27, 3169
Kerr, G. S., Fletcher, L., Russell, A. J. B., & Allred, J. C. 2016, ApJ, 827, 101
Knight, J. W., & Sturrock, P. A. 1977, ApJ, 218, 306
Kolotkov, D. Y., Nakariakov, V. M., & Kontar, E. P. 2018, ApJ, 861, 33
Kontar, E. P., Hannah, I. G., & MacKinnon, A. L. 2008, A&A, 489, L57
Kontar, E. P., Yu, S., Kuznetsov, A. A., et al. 2017, Nature Communications, 8, 1515
Kopp, R. A., & Pneuman, G. W. 1976, SoPh, 50, 85
Krucker, S., Hudson, H. S., Glesener, L., et al. 2010, ApJ, 714, 1108
Krucker, S., Hudson, H. S., Jeffrey, N. L. S., et al. 2011, ApJ, 739, 96
Krucker, S., Hurford, G. J., MacKinnon, A. L., Shih, A. Y., & Lin, R. P. 2008, ApJ, 678, L63
Krucker, S., White, S. M., & Lin, R. P. 2007, ApJ, 669, L49
Kuznetsov, A. A. 2006, SoPh, 237, 153

Kuznetsov, A. A., & Tsap, Y. T. 2007, SoPh, 241, 127
Leibacher, J., Sakurai, T., Schrijver, C. J., & van Driel-Gesztelyi, L. 2010, SoPh, 263, 1
Lemen, J. R., Title, A. M., Akin, D. J., et al. 2012, SoPh, 275, 17
Lin, R. P., Dennis, B. R., Hurford, G. J., et al. 2002, SoPh, 210, 3
Liu, C., Xu, Y., Cao, W., et al. 2016, Nature Communications, 7, 13104
Liu, W., Jin, M., Downs, C., et al. 2018, ApJ, 864, L24
Liu, W., & Ofman, L. 2014, SoPh, 289, 3233
Liu, W.-J., Qiu, J., Longcope, D. W., & Caspi, A. 2013, ApJ, 770, 111
Long, D. M., Bloomfield, D. S., Chen, P. F., et al. 2017, SoPh, 292, 7
McCauley, P. I., Cairns, I. H., & Morgan, J. 2018, SoPh, 293, 132
McCauley, P. I., Cairns, I. H., Morgan, J., et al. 2017, ApJ, 851, 151
McMullin, J. P., Waters, B., Schiebel, D., Young, W., & Golap, K. 2007, in Astronomical Society of the Pacific Conference Series, Vol. 376, Astronomical Data Analysis Software and Systems XVI, ed. R. A. Shaw, F. Hill, & D. J. Bell, 127
Mohan, A., & Oberoi, D. 2017, SoPh, 292, 168
Nakariakov, V. M., Arber, T. D., Ault, C. E., et al. 2004, MNRAS, 349, 705
Nakariakov, V. M., & Melnikov, V. F. 2009, SSRv, 149, 119
Neupert, W. M. 1968, ApJ, 153, L59
Nitta, N. V., Schrijver, C. J., Title, A. M., & Liu, W. 2013, ApJ, 776, 58
Pasachoff, J. M., Babcock, B. A., Russell, K. D., & Seaton, D. B. 2002, SoPh, 207, 241
Patsourakos, S., & Vourlidas, A. 2012, SoPh, 281, 187
Perley, R. A., Chandler, C. J., Butler, B. J., & Wrobel, J. M. 2011, ApJ, 739, L1
Pizer, S., Amburn, E., Austin, J., et al. 1987, Computer Vision, Graphics, and Image Processing, 39, 355
Provornikova, E., Laming, J. M., & Lukin, V. S. 2018, ApJ, 860, 138
Qin, Z., Li, C., Fu, Q., & Gao, Z. 1996, SoPh, 163, 383
Qiu, J., Lee, J., Gary, D. E., & Wang, H. 2002, ApJ, 565, 1335
Qiu, J., Liu, W.-J., & Longcope, D. W. 2012, ApJ, 752, 124
Rausche, G., Aurass, H., Mann, G., Karlický, M., & Vocks, C. 2007, SoPh, 245, 327
Reep, J. W., Bradshaw, S. J., & Holman, G. D. 2016, ApJ, 818, 44
Reep, J. W., & Russell, A. J. B. 2016, ApJ, 818, L20
Reep, J. W., Russell, A. J. B., Tarr, L. A., & Leake, J. E. 2018, ApJ, 853, 101
Reid, M. J., Schneps, M. H., Moran, J. M., et al. 1988, ApJ, 330, 809
Roberts, B., Edwin, P. M., & Benz, A. O. 1983, Nature, 305, 688
—. 1984, ApJ, 279, 857
Rosenberg, H. 1970, A&A, 9, 159
Russell, A. J. B., & Fletcher, L. 2013, ApJ, 765, 81
Russell, A. J. B., & Stackhouse, D. J. 2013, A&A, 558, A76
Scherrer, P. H., Schou, J., Bush, R. I., et al. 2012, SoPh, 275, 207
Sturrock, P. A. 1966, Nature, 211, 695
SunPy Community, T., Mumford, S. J., Christe, S., et al. 2015, Computational Science and Discovery, 8, 014009
Tan, B., Zhang, Y., Tan, C., & Liu, Y. 2010, ApJ, 723, 25
Tarr, L. A. 2017, ApJ, 847, 1
Tomczyk, S., McIntosh, S. W., Keil, S. L., et al. 2007, Science, 317, 1192
van den Oord, G. H. J. 1990, A&A, 234, 496
Van Doorsselaere, T., Gijsen, S. E., Andries, J., & Verth, G. 2014, ApJ, 795, 18
Van Doorsselaere, T., Nakariakov, V. M., & Verwichte, E. 2008, ApJ, 676, L73
Varady, M., Karlický, M., Moravec, Z., & Kašparová, J. 2014, A&A, 563, A51
Vernazza, J. E., Avrett, E. H., & Loeser, R. 1981, The Astrophysical Journal Supplement Series, 45, 635

Veronig, A., Vršnak, B., Dennis, B. R., et al. 2002, A&A, 392, 699

Wang, Z., Chen, B., & Gary, D. E. 2017, ApJ, 848, 77

Warmuth, A. 2015, Living Reviews in Solar Physics, 12, 3

Winglee, R. M., & Dulk, G. A. 1986, ApJ, 307, 808

Wygant, J. R., Keiling, A., Cattell, C. A., et al. 2000, Journal of Geophysical Research, 105, 18,675

—. 2002, Journal of Geophysical Research (Space Physics), 107, 1201

Yu, S., Nakariakov, V. M., Selzer, L. A., Tan, B., & Yan, Y. 2013, ApJ, 777, 159

Zlotnik, E. Y. 2013, SoPh, 284, 579

Zlotnik, E. Y., Zaitsev, V. V., Aurass, H., Mann, G., & Hofmann, A. 2003, A&A, 410, 1011